Frontiers in Heat and Mass Transfer (FHMT), 19, 18 (2022)
DOI: 10.5098/hmt.19.18

Global Digital Central
ISSN: 2151-8629

Frontiers in Heat and Mass Transfer

Available at www.ThermalFluidsCentral.org

STUDY ON THERMAL-HYDRAULIC PERFORMANCE OF THE PRINTED CIRCUIT HEAT EXCHANGER WITH AIRFOIL FINS FOR SUPERCRITICAL LIQUEFIED NATURAL GAS

Yulin Tian[a], Chengyi Long[b], Linghong Tang[a,*]

[a]*School of Mechanical Engineering, Xi'an Shiyou University, Xi'an 710065, Shaanxi, China*
[b]*Wuhan Second Ship Design and Research Institute, Wuhan 430205, Hubei, China*

ABSTRACT

In this study, the thermal-hydraulic performance of eight different printed circuit heat exchanger (PCHE) configurations with supercritical liquefied natural gas as the working fluid are studied by a numerical method. Firstly, the thermal-hydraulic performance of the PCHE with different airfoil fins are investigated at different operating pressures, which indicate that the PCHE with airfoil fins has better thermal performance but worse hydraulic performance when it operates at higher pressure condition. Furthermore, the effects of different airfoil configurations on the thermal-hydraulic performance are analyzed in detail. The results show that asymmetric airfoils can provide better heat transfer performance than symmetrical airfoils. Finally, the overall heat transfer performance of PCHEs is evaluated by the identical mass flow rate criterion, identical pressure drop criterion and identical pumping power criterion, respectively. The results show that NACA 0024, NACA m18 and NACA 23021 airfoil fins exhibit the best comprehensive performance, respectively.

Keywords: *Printed circuit heat exchanger, Airfoil Fins, Thermal-hydraulic performance, Evaluation criteria.*

1. INTRODUCTION

Natural gas (NG) is well-known as one of the cleanest form of fossil fuels, and it is the fastest growing primary energy source owing to its advantages such as clean and efficient combustion, reliable and durable supply, energy and specific density, convenient and clean usage, and flexible implementations (vehicles, power generation plants, industrial and residential usage, etc.) (Smil, 2015). The liquefied natural gas (LNG) technology provides an economically feasible way of transporting NG over long distances and currently accounts for nearly 30% of the international trade of this resource (Popov *et al*., 2019). Floating liquefied natural gas is an alternative LNG supply method, and it is easy to produce, carry and import of the LNG as it is compared to the traditional LNG supply chain for the offshore reserves (Won *et al.*, 2014), and liquefied natural gas-floating production storage and offloading (LNG-FPSO) is a promising energy-efficient method compared to onshore NG treatment facility when the gas source is located in a distant offshore ocean. A further development is the floating regasification units that transform LNG back to NG at the market location, and such units are called liquefied natural gas - floating storage and regasification units (LNG-FSRU). Process technology for LNG-FSRU can be presented as follows: LNG is transferred into cargo tank by dedicated LNG feed pump, then LNG is sent to high pressure booster pump which is used to make high pressure before entering LNG vaporizer, after that LNG will be vaporized and sent to end user (Lee *et al*., 2014). Four main kinds of LNG vaporizers are commercially available, that is, intermediate fluid vaporizer, open rack vaporizer, super open rack vaporizer, and submerged combustion vaporizer. However, the heat exchangers for LNG-FPSO and LNG-FSRU should be more compact than the ones in onshore liquefaction plant due to its limited platform area (Baek *et al*., 2011). Printed circuit heat exchanger (PCHE) is a newly developed heat exchanger with favorable characteristic of compactness, and its potential to further penetrate the market is rather substantial, especially if the heat exchanger size, weight and endurance are major concerns (Popov *et al*., 2019).

The first PCHE was originally developed in 1980 at the University of Sydney, while a major PCHE manufacturer and pioneer is the Heatric company (UK), which is highly specialized in the area since 1985 (Fan and Luo, 2008). PCHEs are manufactured by photochemical etching (Xin *et al*., 2017) and diffusion bonding technologies, and can able to reliably operate under large temperature range (from -200 ℃ to 900 ℃) and high pressure (60 MPa) conditions (Reay *et al.*, 2013). During the past few years, researchers have spent considerable effort to study the thermal-hydraulic performance of PCHEs. The common flow channels of PCHEs are straight channels, wavy channels, zigzag channels, S-shaped channels and channels with airfoils. Chen *et al.* (2016) experimentally investigated the thermal-hydraulic performance of a zigzag channel PCHE in a high temperature helium test facility at the Ohio State University. New thermal-hydraulic correlations for current zigzag channels with rounded bends were developed based on the experimental data. Compared to thermal performance in straight circular pipes, zigzag channels provided a small advantage in the laminar flow regime but significant advantage near the transition flow regime. Considering the huge pressure loss caused by a zigzag channel, Ngo *et al.* (2006) proposed a new channel called the S shaped channel applied to a hot water supplier in which cold water was heat-exchanged with supercritical CO_2, which was found to provide about 3.3 times less volume, and reduced pressure drop by 37% on the CO_2 side and by 10 times on the H_2O side. Ma *et al.* (2015) studied the thermal-hydraulic performance of zigzag-type printed circuit heat

* Corresponding Author. E-mail: lhtang97@163.com

Global Digital Central
ISSN: 2151-8629

exchanger with helium as the working fluid operating at the typical temperature of 900 ℃ in the very high temperature reactor. The results showed that the flow and temperature at high temperature could not achieve a fully-developed condition due to the significant variation of thermal physical properties arisen from the large temperature difference.

Lian *et al.* (2021) considered the difference between the two-side channels, and put forward a new structure for the printed circuit heat exchanger. Compared with the conventional printed circuit heat exchanger, the core volume of the optimized hybrid printed circuit heat exchanger was reduced by 49%, and the heat transfer rate per unit volume was increased by 145%. Xu *et al.* (2022) proposed a simplified mechanical stress method based on homogenization method for PCHE. And proposed an optimized rectangular channel, which had the same mechanical characteristics with a semicircular channel. The mechanical characteristics of the optimized rectangular channel were close to the corresponding semicircular channel, which can benefit for the weight and volume reduction of PCHE. Chang *et al.* (2021) proposed a novel precooler based on printed circuit heat exchanger. Segmented thermal design method and genetic algorithm were used for structure optimization. The results indicated that the novel precooler had higher compactness and volumetric power. Ma *et al.* (2021) established a numerical model to study the thermal-hydraulic characteristics of transcritical natural gas in the printed circuit heat exchanger in rolling conditions. The results showed that the rolling condition had few effects on the total heat transfer rate, but significantly affected the local friction factor and heat transfer characteristics. The rolling condition enhanced the local heat transfer performance of transcritical natural gas. Tsuzuki *et al.* (2007) obtained an optimal flow channel configuration considering the thermal-hydraulic performance by changing the fin shape and angle parametrically. The new configuration had discontinuous fins with an S-shape, similar to a sine curve, in contrast to a conventional continuous zigzag configuration, and the new configuration had one-fifth of the pressure drop compared to the conventional zigzag configuration with equal thermal-hydraulic performance.

Fan *et al.* (2021) investigated the local and global thermal-hydraulic performances of different PCHEs using supercritical LNG and liquid nitrogen by a numerical method. The PCHE channel shapes included straight, zigzag with different sharp, round corners and sinusoidal shapes were compared. The results showed that the sinusoidal channel had the best thermal-hydraulic performance higher than others among the PCHE configurations. Jiang *et al*. (2022) provides a novel design method for optimizing the flow channel profile of PCHE by applying adaptive segmented non-uniform finned microchannels. The results show that the deviation of the entropy generation number between the optimized and validated values for the non-uniform design is very small, much less than that in the uniform design. Moreover, under the premise of the similar heat transfer efficiency, the volume for the PCHE by the non-uniform design can be reduced by 9.3%. Tang *et al.* (2020) studied the thermal and hydraulic performance of supercritical liquefied natural gas (LNG) in a printed circuit heat exchanger (PCHE) with airfoil fins under a rolling condition. Results indicated that the PCHE had better thermal performance but worse hydraulic performance at a lower pressure condition. Zhao *et al.* (2019) numerically investigated the thermal hydraulic performance of supercritical produce liquefied natural gas (LNG) in the zigzag channel of PCHE. They discussed the effect of the channel bend angle, mass flux and inlet pressure on local convection heat transfer coefficient, and pressure drop. The results showed that the supercritical LNG has a better heat transfer performance when bend angle is less than 15 with the mass flux ranging from 207.2 kg/(m^2·s) to 621.6 kg/(m^2·s). The heat transfer performance was better at larger mass flux and lower operating pressures. Jiang *et al.* (2022) numerically investigated the thermal–hydraulic characteristics of trans-critical NG through the improved staggered S-shaped fin channels. The results showed that except for a few data points across critical temperature affected by entrance effect, the peak HTC always appeared in the vicinity of the pseudo-critical points. Additionally, the simulated results also agreed with the predictions from Ngo correlation.

Kim *et al.* (2008) designed an airfoil fin to optimize the thermal-hydraulic performance of a PCHE. The pressure drop of the airfoil fin could be reduced to one-twentieth of that of the zigzag channel but the total heat transfer rate per unit volume was almost the same. Yoon *et al.* (2014) compared the overall heat transfer performance of four different PCHEs, which were straight, zigzag, S-shape, and airfoil PCHEs. The comparison results showed that the airfoil PCHEs provided the best overall heat transfer performance. From the above review, it was concluded that the thermal performance may be enhanced by non-straight channels, especially channels with airfoil fins. The PCHEs with airfoil fins received a lot of attention because of their good heat transfer performance. Xu *et al.* (2015) numerically investigated the effect of four discontinuous fin configurations (rectangle fin, rounded rectangle fin, ellipse fin, and airfoil fin) in inline and staggered arrangements on the thermal-hydraulic performance of a PCHE with supercritical CO_2 as the working fluid. The results showed that fin configurations had little effect on the overall heat transfer performance, and the flow resistance dramatically increased during the heating process due to velocity increment caused by the decrease of density but was not significantly affected by the change in dynamic viscosity. Ma *et al.* (2015) numerically studied the effect of the fin-endwall fillet on the thermal-hydraulic performance of a PCHE with airfoil fins. It was found that the fin-endwall fillet could increase heat transfer and pressure drop in the cases with the non-dimensional longitudinal pitch being 1.63. The effect of fin-endwall fillet on the thermal-hydraulic performance decreased with the increase of transverse pitch, but the longitudinal pitch had little effect when the non-dimensional longitudinal pitch was greater than 1.88. Cui *et al*. (2018) proposed two novel fins based on the configuration of National Advisory Committee for Aeronautics (NACA) 0020 airfoil, to further improve the performance of a zigzag channel PCHE with airfoil fins. Chu *et al*. (2020) numerically investigated thermal-hydraulic performances of PCHEs with cambered NACA four-digit airfoil fins used as the condenser in a supercritical CO_2 Brayton power cycle.

According to the studies above, the previous researches mainly focused on investigating the applicability of fin structure, but limited studies have been done to explore the method of optimizing the configurations of different fins types applied in a PCHE. In this study, based on a numerical study of the influence of different airfoil fin types on the thermal-hydraulic performance in a PCHE using supercritical LNG as a working fluid, ways to improve the thermal-hydraulic performance and the direction of optimizing the fin structure are revealed. The results may provide a practical guidance on the heat transfer enhancement method for LNG vaporization devices in the supercritical LNG heat exchange process.

2. NUMERICAL METHOD

2.1 Physical Properties and Date Reduction

Methane is the major chemical component of LNG. As is well known, gas exists as a single-phase medium when the pressure and temperature is above the critical state, so the phase change phenomenon of methane no longer happens when its pressure and temperature is above 4.59 MPa and 190.56 K. The thermal-physical properties of methane, i.e., specific heat c_p, density ρ, thermal conductivity λ and viscosity μ, are calculated by REFPROP at different pressures (7.0 MPa, 8.0 MPa, and 9.0 MPa, respectively). In comparison with the traditional fluid flow and heat transfer behavior, the thermal-physical properties of supercritical methane change dramatically with temperature as shown in Fig. 1. The variations of the thermal-physical properties with temperature can be expressed by the user defined function (UDF) function in ANSYS FLUENT 19.0, and the deviations between data from REFPROP and the computed data by UDF are within ±2%.

The Reynolds number (Re) is defined as

$$Re = \frac{\rho u_{\max} D_h}{\mu} = \frac{mD_h}{\mu A_{\min}} \quad (1)$$

Global Digital Central
ISSN: 2151-8629

where u_{max} is the velocity of methane evaluated at the minimum cross-section, m is the mass flow rate, and A_{min} is the minimum cross-section in the channel. ρ is the density of methane, and μ is the dynamic viscosity of methane, which are evaluated at the mean temperature of methane. D_h is the hydraulic diameter and is defined by

$$D_h = \frac{4A_{min}}{P} \tag{2}$$

where P is the perimeter.

The local Nusselt number (Nu_L) is defined as

$$Nu_L = \frac{h_L D_h}{\lambda_L} \tag{3}$$

The mean Nusselt number ($\overline{Nu}$) is defined as

$$\overline{Nu} = \frac{1}{n}\sum_{i=1}^{n} Nu_L = \frac{1}{n}\sum_{i=1}^{n} \frac{mc_{p,i}(t_{i+1}-t_i)D_h}{\lambda_i \Delta T_i} \tag{4}$$

in which, the local logarithmic mean temperature difference ΔT_i is defined as

$$\Delta T_i = \frac{t_{i+1}-t_i}{\ln(\frac{t_w - t_i}{t_w - t_{i+1}})} \tag{5}$$

where h_L is the local heat transfer coefficient, n is the total cross section number. t_i is the temperature of methane in the i cross section, t_w is the temperature of the top and bottom surfaces of the local passage. λ_i is the thermal conductivity and $c_{p,i}$ is the specific heat, which are evaluated at the mean temperature of methane in the local passage.

The Darcy friction factor (f-factor) can reflect the pressure drop of the channel and is given as

$$f = \frac{2\Delta p_f D_h}{\rho (u_{max})^2 L_2} \tag{6}$$

where Δp_f is the frictional pressure drop and L_2 is the length of the channels. The frictional pressure drop Δp_f can be obtained by

$$\Delta p_f = \Delta p - \Delta p_a \tag{7}$$

$$\Delta p_a = \rho_{out}(u_{out})^2 - \rho_{in}(u_{in})^2 \tag{8}$$

where Δp is the total pressure drop, and Δp_a is the acceleration pressure drop. ρ_{in}, u_{in} and ρ_{out}, u_{out} are the density and velocity evaluated at the inlet and outlet of the channels, respectively.

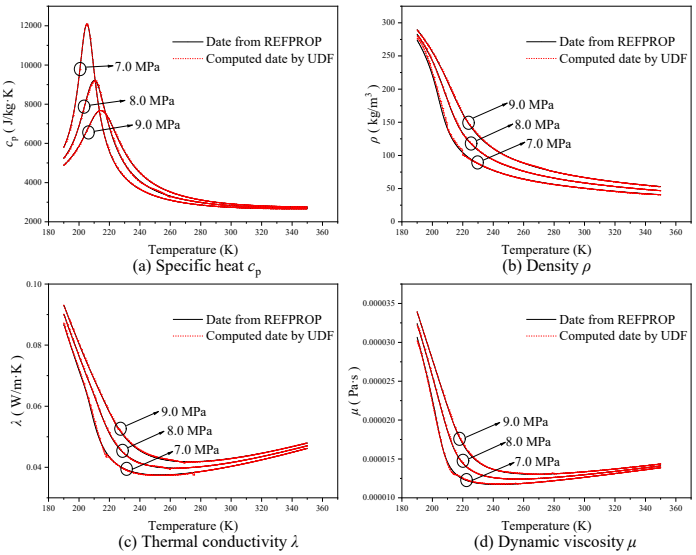

Fig. 1 Thermal-physical properties of methane at different pressure

2.2 Physical Model

A three-dimensional heat exchanger unit is designed to implement the numerical simulations, as shown in Fig. 2 (a). The methane-flow is described in a coordinate system, in which x, y, z are streamwise, spanwise, and normal coordinates, respectively. The channel height H is 1.0 mm, and the channel width W is 2.0 mm. Since the PCHE with airfoil fins was first proposed by Kim (Kim *et al*., 2008) in 2008, its excellent overall heat transfer performance has gained more and more attentions. A 4-digit NACA airfoil fin is determined by three dimensions: the height (H_f), the maximum thickness (W_f) and the chord length (L_f), as shown in Fig. 2 (b) and (c). From the mechanism of chemical etching, processing cost does not increase with the complexity of the airfoil structure, which ensures the availability of airfoil fins. However, considering the operability of chemical etching, the channel depth is kept at 0.5-1.0 mm (etched deeper, more serious side etching) (Xu *et al*., 2014). In this study, H_f = 1 mm, and L_f = 4 mm. In order to support a uniform velocity at the inlet and suppress the backflow at the outlet, the inlet and the outlet are both extended to 16 times of the channel height. Therefore, the channel lengths (L_1, L_2, L_3) are 16.0 mm, 64.0 mm and 16.0 mm, respectively.

In this study, seven different airfoils are compared: NACA 0024, NACA 2421, NACA 23021, NACA 4418, NACA 63, NACA m18 and NACA m21. The geometric parameters are listed in Table 1.

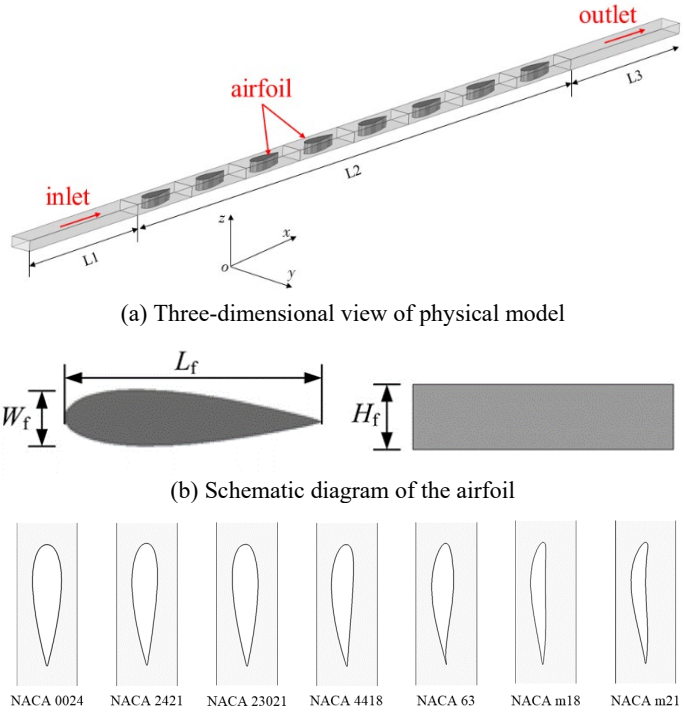

(a) Three-dimensional view of physical model

(b) Schematic diagram of the airfoil

(c) Top view of seven different airfoil structures

Fig. 2 Physical model of the PCHE with airfoil

2.3 Numerical method

The governing equations for continuity, momentum and energy may be expressed in tensor notation as

$$\nabla \cdot (\rho \vec{U} \phi) = \nabla \cdot (\Gamma_\phi \nabla \phi) + S_\phi \tag{9}$$

In the above equation, the dependent variable, ϕ, stands for the velocity components, temperature, k and ε. The terms Γ_ϕ and S_ϕ represent the appropriate diffusion coefficients and the source terms, respectively. The particular expressions for ϕ, Γ_ϕ and S_ϕ (Versteeg, 2007) are summarized in Table 2.

Global Digital Central
ISSN: 2151-8629

Table 1 Geometric parameters of different PCHE configurations

Parameter	Symbol/unit	NACA 0024	NACA 2421	NACA 23021	NACA 4418	NACA 63	NACA m18	NACA m21
Channel length	L_2/mm	64.0	64.0	64.0	64.0	64.0	64.0	64.0
Channel width	W/mm	2.0	2.0	2.0	2.0	2.0	2.0	2.0
Channel height	H/mm	1.0	1.0	1.0	1.0	1.0	1.0	1.0
Max airfoil thickness	W_f/mm	0.96	0.84	0.84	0.72	0.71	0.48	0.48
Airfoil chord length	L_f/mm	4.0	4.0	4.0	4.0	4.0	4.0	4.0
Airfoil height	H_f/mm	1.0	1.0	1.0	1.0	1.0	1.0	1.0
Row	N	8	8	8	8	8	8	8

Table 2 Expressions for ϕ, Γ_ϕ and S_ϕ

ϕ	Γ_ϕ	S_ϕ
1	0	0
u	$\mu+\mu_t$	$S_u=-\frac{\partial p}{\partial x}+\frac{\partial}{\partial x}\left((\mu+\mu_t)\frac{\partial u}{\partial x}\right)+\frac{\partial}{\partial y}\left((\mu+\mu_t)\frac{\partial v}{\partial x}\right)+\frac{\partial}{\partial z}\left((\mu+\mu_t)\frac{\partial w}{\partial x}\right)$
v	$\mu+\mu_t$	$S_v=-\frac{\partial p}{\partial y}+\frac{\partial}{\partial x}\left((\mu+\mu_t)\frac{\partial u}{\partial y}\right)+\frac{\partial}{\partial y}\left((\mu+\mu_t)\frac{\partial v}{\partial y}\right)+\frac{\partial}{\partial z}\left((\mu+\mu_t)\frac{\partial w}{\partial y}\right)$
w	$\mu+\mu_t$	$S_w=-\frac{\partial p}{\partial z}+\frac{\partial}{\partial x}\left((\mu+\mu_t)\frac{\partial u}{\partial z}\right)+\frac{\partial}{\partial y}\left((\mu+\mu_t)\frac{\partial v}{\partial z}\right)+\frac{\partial}{\partial z}\left((\mu+\mu_t)\frac{\partial w}{\partial z}\right)$
t	$\mu/Pr+\mu_t/\sigma_t$	S_t
k	$\mu+\mu_t/\sigma_k$	$S_k=\rho G_k-\rho\varepsilon$
ε	$\mu+\mu_t/\sigma_\varepsilon$	$S_\varepsilon=\frac{\varepsilon}{k}(c_1\rho G_k-c_2\rho\varepsilon)$

where $G_k=\frac{\mu_t}{\rho}\left(\left(\frac{\partial u}{\partial x}\right)^2+\left(\frac{\partial v}{\partial y}\right)^2+\left(\frac{\partial w}{\partial z}\right)^2+\left(\frac{\partial u}{\partial y}+\frac{\partial v}{\partial x}\right)^2+\left(\frac{\partial u}{\partial z}+\frac{\partial w}{\partial x}\right)^2+\left(\frac{\partial v}{\partial z}+\frac{\partial w}{\partial y}\right)^2\right)$, $\mu_t=c_\mu\rho k^2/\varepsilon$, c_μ=0.09, c_1=1.44, c_2=1.92, σ_t=0.85, σ_ε=1.3, σ_k=1.0.

The supercritical methane-flow in the computational domain is regarded as three-dimensional, incompressible, turbulent and quasi-steady. The boundary conditions for computational model are shown in Fig. 3. The flow channels formed by the fins are symmetrical in the longitudinal direction, so the symmetry condition is used for the *x*-*z* plane in this study. The flow velocity u_{in} is assumed to be uniform, the temperature t_{in} is taken as 195 K, and pressure is specified at the outlet of the channels. On the solid surfaces, no-slip conditions are used, and a constant temperature of 340 K is applied at the top and bottom surfaces of the channels. The temperature distribution in the fins will be determined by solving the conjugated heat transfer problem between supercritical methane and the fins in the computational domain.

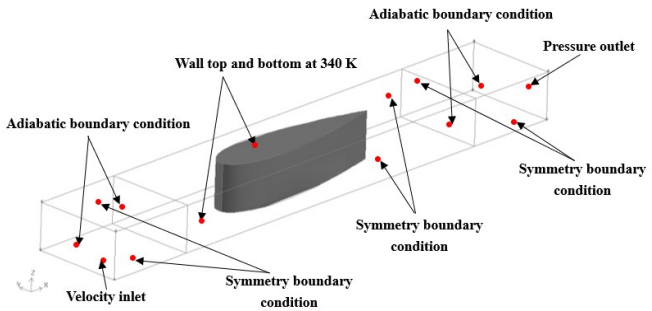

Fig. 3 Boundary conditions for computation model

The foregoing governing equations and boundary conditions are solved by Ansys Fluent 19.0. A preprocessor Gambit 2.4 is used to mesh the computational domain for the solver. In order to control the mesh number and improve the grid quality, a hexahedral grid is used for meshing as shown in Fig. 4. Due to the stringent requirements for boundary grid density under supercritical flow and heat transfer, five boundary layers are used near the top and bottom walls and fin surfaces, with the thickness of the first layer being 0.01 mm.

All variables, including velocity components, pressure and temperature, are averaged to a control volume. The coupling between pressure and velocity is implemented by the semi-implicit method for pressure-linked equations (SIMPLE) algorithm. The quadratic upstream interpolation for convective kinematics (QUICK) method is used to discretize the convection terms. The residuals are set to be less than 10^{-5} and 10^{-8} for continuity and energy equations, respectively, to ensure convergence of the computations. After validating the solution independence of the grid number, the reference grid systems for the PCHE with airfoil fins are about 1,067,680 cells.

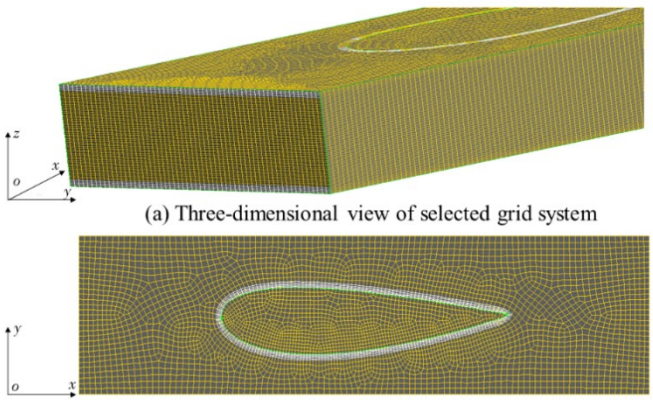

(a) Three-dimensional view of selected grid system

(b) Top view of selected grid system

Fig. 4 Selected grid system

Global Digital Central
ISSN: 2151-8629

2.4 Numerical Method

In order to validate the reliability of the numerical simulation procedure, a model set up from the experiments of Dang and Hihara (2004) is simulated with different turbulence models, i.e., SST *k-ω* turbulence model, standard *k-ε* turbulence model, RNG *k-ε* turbulence model, and realizable *k-ε* turbulence model, at the same operating conditions as in the experiments, and compared with the experimental correlations near the pseudo-critical temperature. The thermal-hydraulic correlations used for comparison are described as

$$\overline{Nu} = \frac{(f_f/8)(Re_b - 1000)Pr}{1.07 + 12.7\sqrt{f_f/8}\,(Pr^{2/3} - 1)} \tag{10}$$

$$Pr = \begin{cases} c_{p,b}\mu_b/\lambda_b, & \text{for } c_{p,b} \geq \overline{c_p} \\ \overline{c_p}\mu_b/\lambda_b, & \text{for } c_{p,b} < \overline{c_p} \text{ and } \mu_b/\lambda_b \geq \mu_f/\lambda_f \\ \overline{c_p}\mu_f/\lambda_f, & \text{for } c_{p,b} < \overline{c_p} \text{ and } \mu_b/\lambda_b < \mu_f/\lambda_f \end{cases} \tag{11}$$

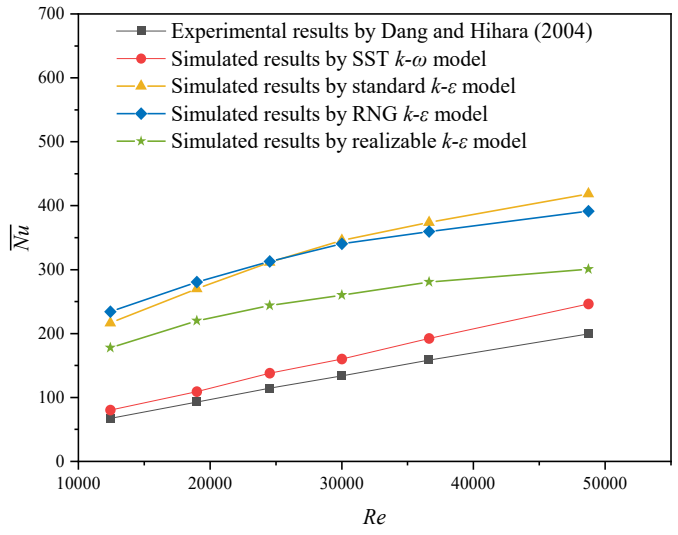

(a) $\overline{Nu}$ comparisons

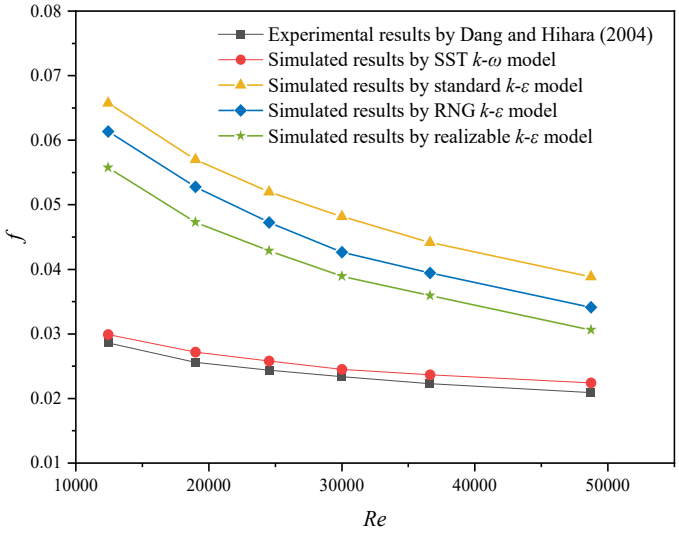

(b) *f*-factor comparisons

Fig. 5 $\overline{Nu}$ and *f*-factor comparisons between simulated and experimental results

$$\overline{c_p} = \frac{h_w^* - h_b^*}{t_w - t_b} \tag{12}$$

$$f_f = (1.82\log_{10}(Re_f) - 1.64)^{-2} \tag{13}$$

$$Re_f = \frac{Gd}{\mu_f} \tag{14}$$

where subscript b represents the mean bulk temperature, and f represents the film temperature. t_f can be obtained by

$$t_f = \frac{t_b + t_w}{2} \tag{15}$$

Figure 5 shows the comparisons between the simulation results and the experimental results. Compared with the experimental results, the mean relative deviations of the Nusselt number and *f*-factor in turn SST *k-ω* turbulence model, are -16.8% and -6.6%, respectively. The simulation results of the SST *k-ω* turbulence model has good agreement with the experimental results, so the SST *k-ω* turbulence model is adopted in this paper.

3. NUMERICAL RESULTS AND DISCUSSION

3.1 Effect of Pressure on The Thermal-Hydraulic Performance

In this study, the pseudo-critical temperature of methane at 7.0, 8.0, and 9.0 MPa is about 205.2, 210.1, and 214.3 K, respectively. From Fig. 1, it can be seen that the temperature of methane along the flow direction in PCHE channels for different cases goes through the pseudo-critical temperature at different operating pressures.

The local thermal and hydraulic performance of NACA 0024 at different operating pressures along the main flow direction is described in Fig. 6.

As shown in Fig. 6, the local Nusselt number Nu_L in the first row is the highest due to the inlet effect, and then the local Nusselt number Nu_L decreases along the main flow direction and reduces to the minimum in the second row. After that, it increases and achieves approximately fully developed condition since the 6th row. The curves of specific heat at different operating pressures show a parabolic distribution along the main flow direction, and specific heat reaches its peak value at the pseudo-critical point. From Fig. 6, it can be seen that the local heat transfer performance is reduced as pressure increases, but it is worth to point out that the local heat transfer performance is enhanced near the pseudo-critical point at different operating pressures.

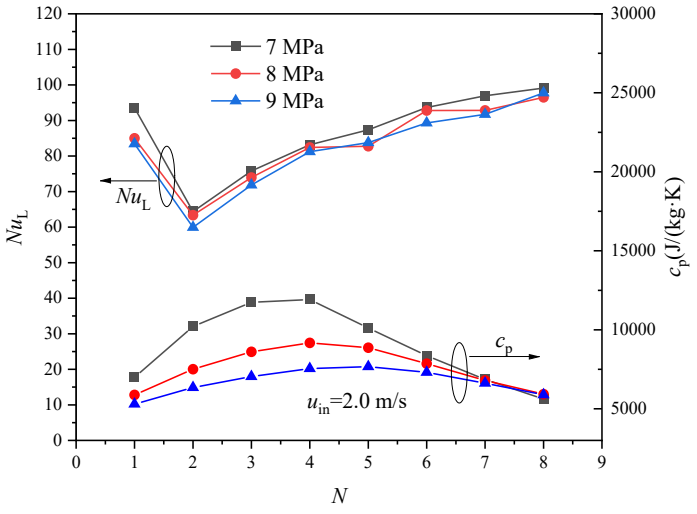

Fig. 6 Local Nusselt number Nu_L and c_p along the main flow direction at u_{in}=2.0m/s.

The average thermal and hydraulic performance of NACA 0024 is compared at different pressures as shown in Fig. 7, where the Reynolds number in the channel is taken as the abscissa. In Fig. 7, it is found that the average Nusselt number $\overline{Nu}$ increases with the increase of Reynolds number, and the heat transfer performance is reduced as pressure increases. This can be explained as follows. The methane velocity is larger at a lower pressure, and the larger velocity can improve the heat transfer performance. On the other hand, the specific heat is larger at a lower pressure in Fig. 6, and the larger specific heat can also greatly improve the capability of supercritical methane for heat transfer enhancement. As a consequence of the above two main reasons, the heat transfer performance is increased as the pressure decreases. Figure 7 also shows the variation of the *f*-factor with the change of inlet velocity at different operating pressures. With the increase of inlet velocity, the *f*-factor decreases. The reason is that the methane velocity is decreased with the increase of pressure, the friction performance is reduced as the operating pressure increases from 7.0 to 9.0 MPa.

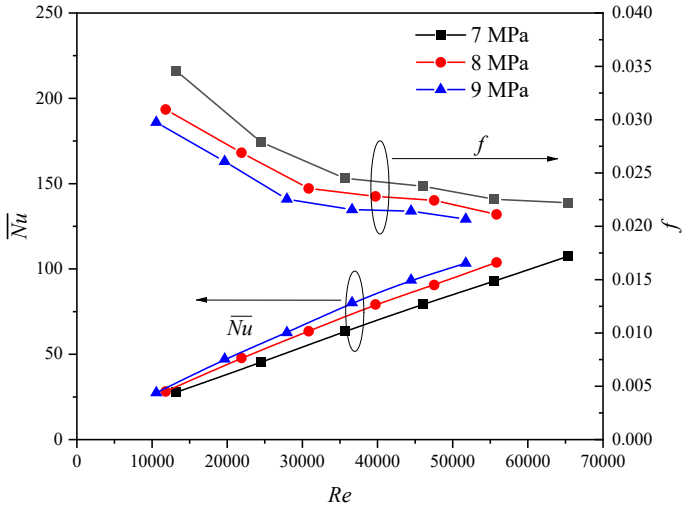

Fig. 7 $\overline{Nu}$ and *f*-factor comparisons at different pressures.

3.2 Thermal-Hydraulic Performance Comparisons for Different Airfoil Configurations

The inlet pressure for different airfoil is set at 8.0 MPa, and the inlet velocities are set at 0.5, 1.0, 1.5, 2.0, 2.5, and 3.0 m/s, respectively. The heat transfer characteristics of different PCHE configurations are compared in Fig. 8 and Fig. 9, where the Reynolds number in channels is taken as the abscissa. As can be seen from Fig. 8 and Fig. 9, the heat transfer performance of different PCHEs increases with the increase of Reynolds number. In this study, only NACA 0024 is a symmetrical airfoil structure, and the other six airfoils are asymmetric. Compared with all airfoils, asymmetrical airfoils have better heat transfer performance than symmetrical airfoils. Due to the similar structure of NACA m18, NACA m21 and NACA 4418, the heat transfer performance of them are almost the same. Similarly, the heat transfer performance of NACA 2421, NACA 63 and NACA 23021 are also almost the same. Compared with NACA 0024, the thickness of NACA m18 is smaller. As is known, the velocity increases when the area of minimum cross-section decreases at the same mass flow rate. Therefore, the heat transfer performance of NACA m18 is better than that of NACA 0024. At the same inlet velocity, NACA m21 provides the best effectiveness of the heat transfer enhancement, the next is NACA 4418, then NACA m18, NACA 0024, NACA 2421, NACA 63 in descending order, and the last one is NACA 23021.

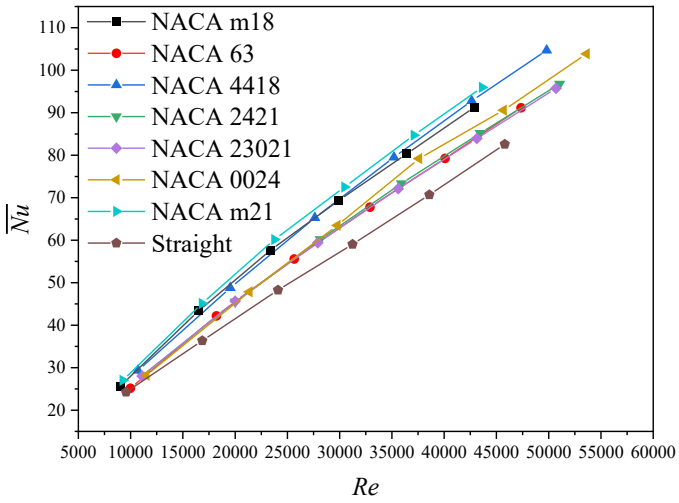

Fig. 8 $\overline{Nu}$ comparisons for different airfoil configurations.

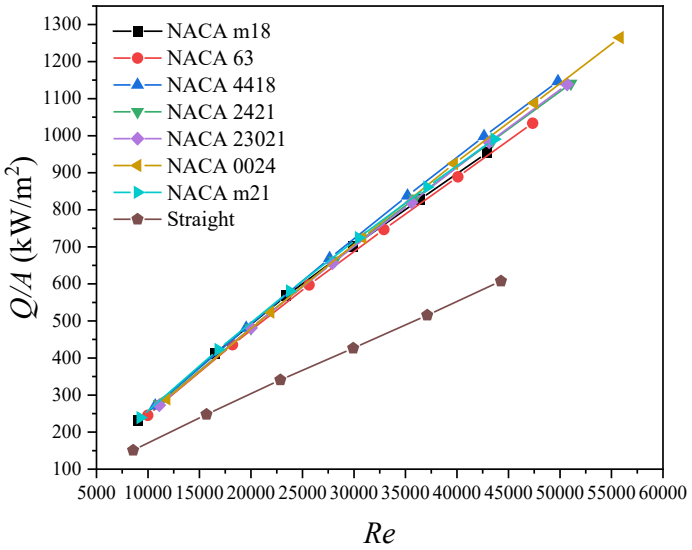

Fig. 9 Heat transfer rate per unit area (*Q*/*A*) comparisons for different airfoil configurations.

Figure 10 shows the streamlines at the central cross section in the *z*-direction of NACA 0024 at u_{in}=1.5 m/s. From Fig. 10, it can be observed that the flow direction of supercritical methane upstream the airfoil is almost parallel to the *x*-direction, then the flow direction is changed and consistent with the direction of the airfoil surface. Figure 11 shows the streamlines in the 8th row of other airfoils along the main flow direction at u_{in}=1.5 m/s. It can be seen from previous studies that the increase of the flow rate can greatly improve the effect of supercritical methane to enhance heat transfer. Comparing NACA 4418 and NACA 63, it can be found that the former has a higher velocity along the airfoil fins, and the heat transfer effect of NACA 4418 is significantly better than that of NACA 63. It can also be seen from Fig. 8 that comparing NACA m18 and NACA m21, the heat transfer performance of both is almost the same. It can be seen that NACA m21 has a more complex structure and a higher velocity along the airfoil, and also has a higher airfoil velocity. It has good heat transfer performance. Comparing NACA m21 and NACA 0024, it can be found that NACA 0024 has a higher velocity along the airfoil fins, but the heat transfer enhancement performance is not as good as that of NACA m21.

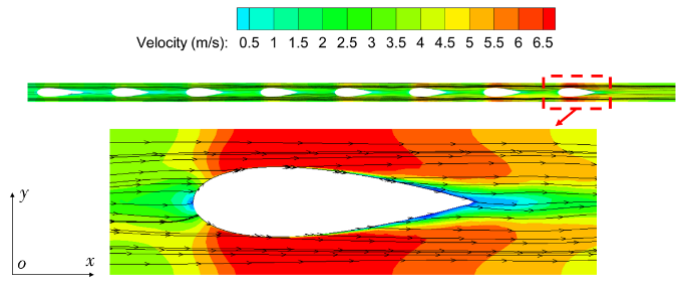

Fig. 10 Streamlines at the central cross section in the *z*-direction of NACA 0024 at u_{in}=1.5 m/s.

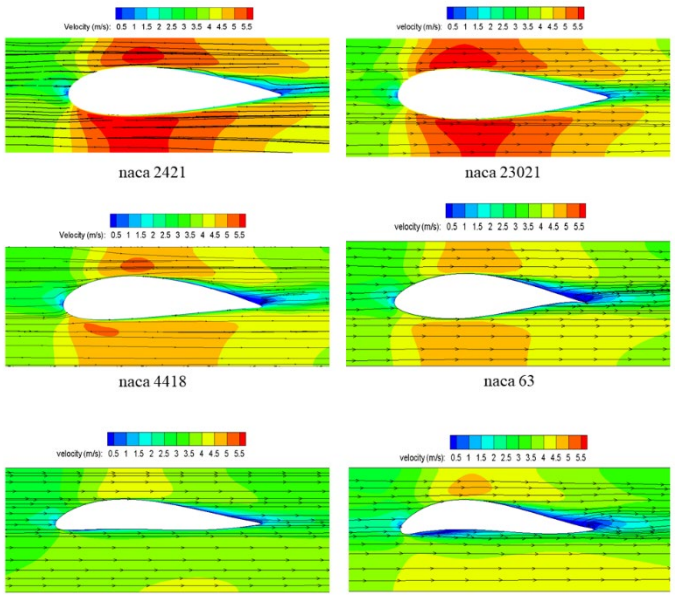

Fig. 11 Streamlines in the 8th row for different airfoil configurations at u_{in}=1.5 m/s.

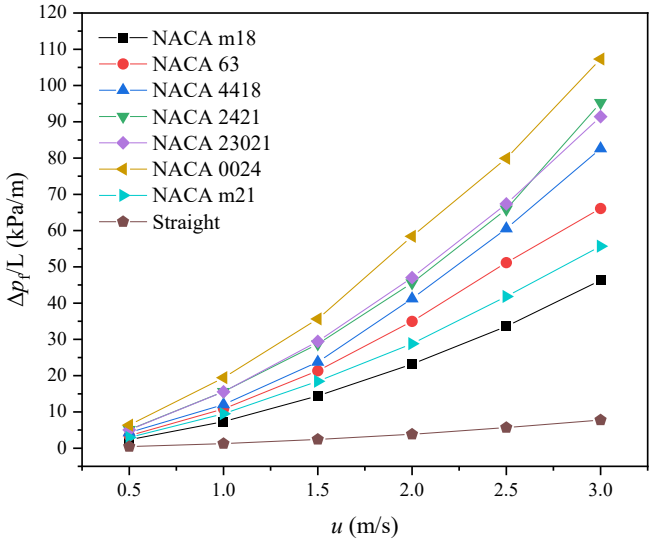

Fig. 12 Variation of pressure drop per unit length for different airfoil configurations.

Figure 12 and Figure 13 illustrate the variations of friction factor for all airfoils above. The *f*-factor decreases with the increase of inlet velocity. The flow resistance of supercritical methane from the inlet to outlet of the channel with airfoils is composed by the acceleration resistance of supercritical methane, the frictional resistance of the channel surfaces and the local resistance of the airfoils, and the local resistance of the airfoils plays a dominant part of the total pressure drop. The results show that the flow resistance of the symmetrical airfoil is the largest, and the flow resistance of the asymmetrical airfoil is the smallest. Because of the maximum airfoil thickness: NACA m21 < NACA 4418 < NACA 2421 < NACA 0024. the hydraulic performance of NACA 0024 and NACA 2421 is worse than that of NACA 4418 and NACA m21. This means that simply increasing the airfoil thickness to obtain a higher fin speed along the airfoil cannot continuously improve the comprehensive heat transfer performance, and the actual heat transfer area and flow resistance should also be considered.

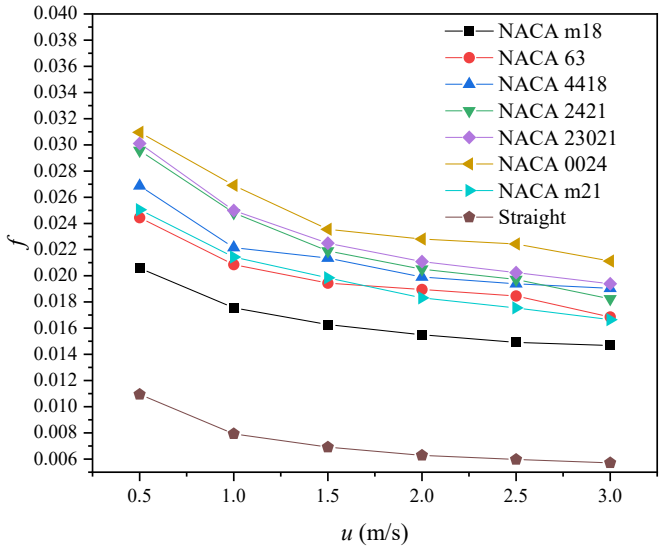

Fig. 13 Friction factor performance comparisons for different airfoil configurations.

3.3 Comprehensive Evaluation of the Overall Heat Transfer Performance

As mentioned above, it is found that different airfoils have different effects on heat transfer and flow characteristics. As usual, the enhancement of heat transfer is always accompanying with the increase of pressure drop. So, in order to compare the performance of heat exchangers, attention is now turned to the comprehensive evaluation of the seven different airfoils in this section. And identical mass flow rate criteria, identical pressure drop criteria and identical pumping power criteria are used. These criteria were successfully used by Yu *et al.* (1999), Wang *et al.* (2001) Tang *et al.* (2009). and Wang *et al.* (2007). Based on the constant thermal properties assumption, the above constrains and the same characteristic length, the formulations of these criteria are given as follows.

(a) Identical mass flow rate criterion (IMF):

$$(ReA_{c,min}/D_c)_c = (\mathrm{Re}\,A_{r,min}/D_r)_r \quad (16)$$

where the subscript ''c'' stands for the compared airfoil structure (NACA 4418, NACA 0024 *et al.*) and the subscript ''r'' means the reference airfoilless straight channel (Straight Channel).

(b) Identical pressure drop criterion (IPD):

$$(f_c Re^2/D_c^3)_c = (f_r Re^2/D_r^3)_r \quad (17)$$

(c) Identical pumping power criterion (IPP):

$$(f_c Re^3 A_{c,min}/D_c^4)_c = (f_r Re^3 A_{r,min}/D_r^4)_r \quad (18)$$

Figure 8 and Figure 13 show the correlations of *Nu* with *Re* and *f* with *Re* for different airfoils. All the correlative expressions of the coefficients are acquired by the linear fitting methods in the logarithmic coordinates. Besides, Correlations and Relative error for different airfoil

Global Digital Central
ISSN: 2151-8629

configurations are shown in Table 3. The ratio of the heat transfer rate between the compared different airfoils and the reference channel may be calculated by Eq. (19) with the constant thermal properties and the same temperature difference between the fluid and the wall. Then we may obtain

$$\frac{Q_c}{Q_r} = \frac{\left[Nu(Re)\cdot A_o/D_c\right]_c}{\left[Nu(Re)\cdot A_o/D_c\right]_r} \tag{19}$$

where $Nu(Re)$ represents the correlation of Nusselt number vs. Reynolds number.

The Reynolds number (Re) of straight channel is taken as the x-coordinate and the heat transfer rate Q_n/Q_{str} is the y-coordinate. The symbols n=NACA 0024, n = NACA 2421 and n= NACA 23021 stand for the ratios of the heat transfer rate of NACA 0024, NACA 2421 and NACA 23021 over that of straight channel, respectively.

Table 3 Correlations and Relative error for different airfoil configurations.

	Correlations	Re	Relative error
Straight Channel	$Nu = 0.0371Re^{0.729}$	8500-44000	-0.25%
	$f = 0.459/Re^{0.415}$		-0.14%
NACA 0024	$Nu = 0.0185Re^{0.839}$	11000-56000	-0.58%
	$f = 0.306/Re^{0.245}$		0.33%
NACA 2421	$Nu = 0.0162Re^{0.802}$	11000-51000	0.0038%
	$f = 0.549/Re^{0.313}$		0.26%
NACA 23021	$Nu = 0.016Re^{0.802}$	11000-51000	-0.74%
	$f = 0.359/Re^{0.267}$		0.57%
NACA 4418	$Nu = 0.017Re^{0.807}$	10000-50000	0.26%
	$f = 0.218/Re^{0.228}$		-0.85%
NACA 63	$Nu = 0.0142Re^{0.814}$	9000-47000	-0.22%
	$f = 0.14/Re^{0.193}$		0.06%
NACA m18	$Nu = 0.0246Re^{0.771}$	9000-42000	1.51%
	$f = 0.115/Re^{0.194}$		-0.80%
NACA m21	$Nu = 0.022Re^{0.785}$	9200-43000	1.25%
	$f = 0.282/Re^{0.264}$		0.49%

Figure 14 shows the heat transfer performance comparisons for different airfoil configurations in identical mass flow rate criterion. It can be found from Fig. 14 that, the heat transfer rates for all airfoils are higher than 1. The heat transfer rate of all the airfoils increased with the increase of Reynolds number. From Fig. 14, NACA 0024 provides the best effectiveness of the heat transfer enhancement, the next is NACA 4418, then NACA 2421, NACA 23021, NACA 63, NACA m21 in descending order, and the last one is NACA m18. The reason can be explained as follows. The minimum cross-section area of the channel decreases as the airfoil maximum thickness increases, and the fluid velocity at the minimum cross-section increases at the same volume flow rate. Therefore, the local heat transfer performance at the minimum cross-section is enhanced, and this can improve the total heat transfer performance in the channel, but the corresponding pressure drop is also increased.

It can be seen clearly that from Fig. 15, the heat transfer rates are all less than 1 in identical mass flow rate criterion. It means that the comprehensive heat transfer performance of straight channel is the best among the eight PCHE configurations. Among the seven airfoil configurations, the heat transfer performance of NACA m18 are best than those of the other six airfoils, the next is NACA 4418, then NACA 63, NACA 2421, NACA 23021, and NACA 0024, the last one is NACA m21. the penalty of pressure drop is increased with the increase of airfoil maximum thickness. That is to say, NACA m18 is the best choice for situations where enhanced heat transfer and reduced pressure loss are required.

For identical pumping power criterion, it can be seen clearly that from Fig. 16, the heat transfer rates are all less than 1. Among the seven airfoil configurations, the heat transfer performance of NACA m18 are best than those of the other six airfoils, the next is NACA 4418, then NACA 63, NACA 2421, NACA 23021, and NACA 0024, the last one is NACA m21. On the whole, it can be found that more consideration is given to the influence of economic factors on the heat transfer effect under pumping power criterion, the comprehensive heat transfer performance of NACA m18 is the best.

The above comprehensive comparison definitely shows that for the PCHE with different airfoils configurations, the effects of the airfoils on the overall performance are completely different. It can be found that in the present study, the performances of the airfoil configurations for PCHE are better than straight channel.

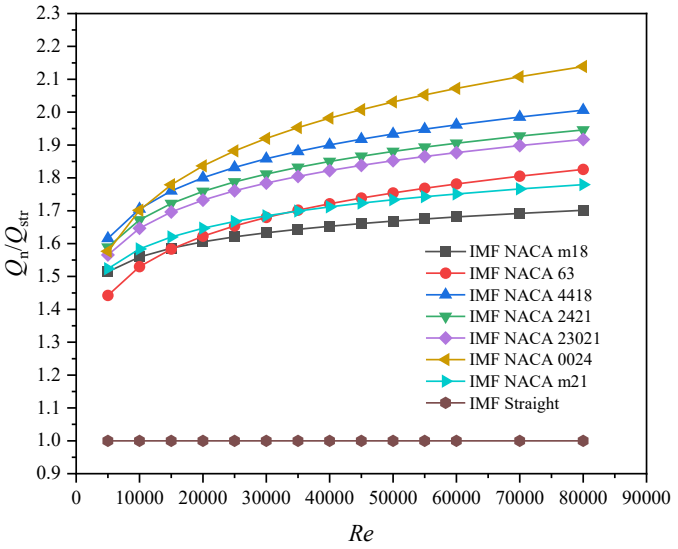

Fig. 14 Heat transfer performance comparisons for different airfoil configurations in IMF.

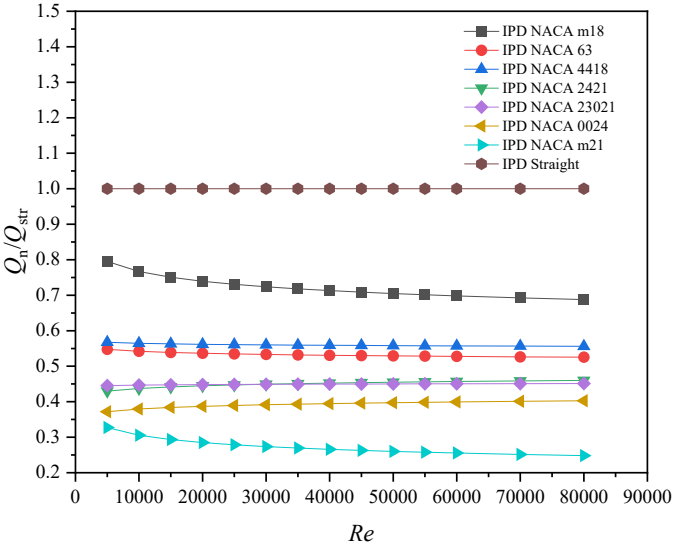

Fig. 15 Heat transfer performance comparisons for different airfoil configurations in IPD.

Global Digital Central
ISSN: 2151-8629

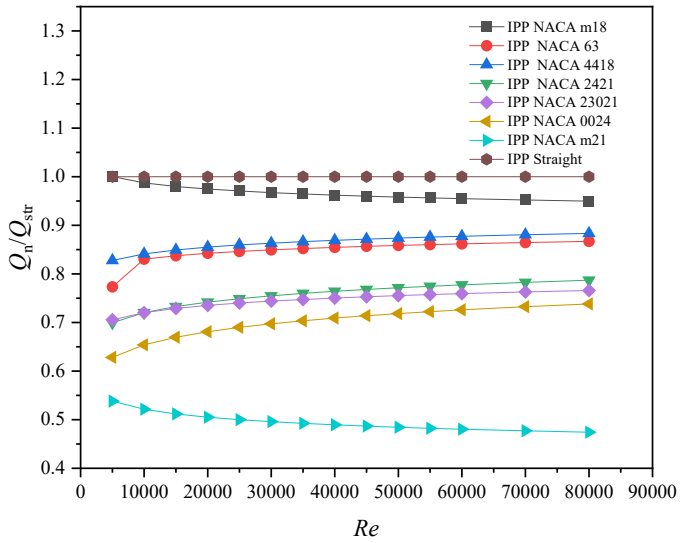

Fig. 16 Heat transfer performance comparisons for different airfoil configurations in IMF.

If the pressure drop factor is not considered, the thickness becomes the main factor affecting the comprehensive heat transfer performance. This means that increasing the airfoil thickness can improve the comprehensive heat transfer performance. The best comprehensive heat transfer performance is NACA 0024, the next is NACA 4418, NACA 2421, NACA 23021, NACA 63, NACA m21, the last one is NACA m18. Considering the pressure drop factor, reducing the thickness can obtain better comprehensive heat transfer performance. The NACA m18 becomes the best, the next is NACA 4418, NACA 63,NACA 2421, NACA 23021, NACA 0024, and the last one is m21.

4. CONCLUSIONS

This article compares the effects of seven different airfoil configurations on the heat transfer and flow friction characteristics for supercritical LNG by three dimensional numerical simulations. Main conclusions can be summarized as follows:

(1) At the same inlet velocity, the effects of different heat transfer enhancement models are concluded such that NACA 4418 > NACA 0024 > NACA 2421 > NACA 23021 > NACA m21 > NACA m18 > NACA 63 > Straight channel. The comparative results of all airfoil configurations can indicate that asymmetric airfoils can provide better heat transfer performance than symmetrical airfoils. This means that the structure of asymmetric airfoils should be properly designed in order to further enhance heat transfer.

(2) Moreover, the comparative results indicate that the *f*-factors of NACA 2421 and NACA 4418 are smaller than that of NACA 0024. the hydraulic performance of NACA 0024 and NACA 2421 is worse than that of NACA 4418. This means that simply increasing the airfoil thickness to obtain a higher fin speed along the airfoil cannot continuously improve the comprehensive heat transfer performance, and the actual heat transfer area and flow resistance should also be considered.

(3) Comprehensive comparisons of heat transfer performance for the PCHE under different airfoil configurations are evaluated with three criteria. It can be found that the PCHE with different airfoils configurations has completely different effects on the overall performance for different heat exchangers. For identical mass flow rate criterion, NACA 0024 provides the best effectiveness of the heat transfer enhancement, the next is NACA 4418, then NACA 2421, NACA 23021, NACA 63, NACA m21, in descending order, and the last one is NACA m18. For identical pressure drop criterion, among the seven airfoil configurations, the heat transfer performance of NACA m18 are best than those of the other six airfoils, the next is NACA 4418, then NACA 63, NACA 2421, NACA 23021, and NACA 0024, the last one is NACA m21. Therefore, the penalty of pressure drop is increased with the increase of airfoil maximum thickness. For identical pumping power criterion, it can be found that more consideration is given to the influence of economic factors on the heat transfer effect under pumping power criterion, the comprehensive heat transfer performance of NACA m18 is the best.

ACKNOWLEDGEMENTS

This work is supported by the Postgraduate Innovation and Practice Ability Development Fund of Xi'an Shiyou University (YCS21211050), the Open Fund of Science and Technology on Thermal Energy and Power Laboratory (TPL2020B02), and the Natural Science Basic Research Plan in Shaanxi Province of China (No. 2021JQ-578).

NOMENCLATURE

A	area, m^2
A_{min}	minimum flow area, m^2
A_o	total heat transfer area, m^2
c_p	specific heat at constant pressure, J/(kg·K)
d	inner diameter, mm
D_h	hydraulic diameter, m
f	Darcy friction factor
G	mass flux, kg/(m^2·s)
G_k	generation of turbulence kinetic energy, kg/(m·s^3)
h*	enthlpy, J/kg
h	heat transfer coefficient, W/(m^2·K)
H	channel height, mm
H_f	airfoil height, mm
k	overall heat transfer coefficient, W/(m^2·K)
L	length of front area
L_1, L_2, L_3	channel length, mm
L_f	airfoil chord length, mm
m	mass flow rate, kg/s
n	total cross section number
N	number of fin rows
NACA	National Advisory Committee for Aeronautics
Nu	Nusselt number
$\overline{Nu}$	mean Nusselt number
Nu_L	local Nusselt number
p	pressure, Pa
P	perimeter, mm
PCHE	printed circuit heat transfer
Pr	Prandtl number
Q	heat transfer rate, W
Re	Reynolds number
SST	shear stress transport
S_ϕ	source tern, W/m^3
t	temperature, K
u, v, w	x, y, z velocity components, m/s
UDF	user defined function
W	width of front area, m
W_f	maximum airfoil thickness, mm
x, y, z	Cartesian co-ordinates

Greek Symbols

Γ_ϕ	diffusion coefficient, m^2/s
Δp	total pressure drop, Pa
Δp_a	acceleration pressure drop, Pa
Δp	frictional pressure drop, Pa
Δt	temperature difference, K
ΔT	logarithmic mean temperature difference, K
ε	dissiaion rate, 1/s
δ	thickness, m
λ	thermal conductivity, W/(m·K)
μ	dynamic viscosity of fluid, kg/(m·s)
μ_t	turbulent eddt-viscosity, kg/(m·s)

ρ	density, kg/m^3
σ	contraction ratio of the fin array
σ_k, σ_t, σ_ε	turbulence model constant
ϕ	dependent variable
ω	specific dissipation rate, 1/s

Subscripts

b	mean value
f	fin, frictional, film temperature
in	inlet
L	local
max	maximum value
min	minimum value
out	outlet
r	reference value
str	straight channel without airfoil
w	wall

REFERENCES

Chang, H. L., Lian, J., Ma, T., Li, L., and Wang, Q.W., 2021, "Design and Optimization of an Annular Air-Hydrogen Precooler for Advanced Space Launchers Engines," *Energy Conversion and Management*, **241**, 114279.
https://doi.org/10.1016/j.enconman.2021.114279

Chen, M. H., Sun, X. D., Christensen, R. N., Skavdahl, I., Utgikar, V., and Sabharwall, P. 2016, "Pressure Drop and Heat Transfer Characteristics of a High-Temperature Printed Circuit Heat Exchanger," *Applied Thermal Engineering*, **108**, 1409-1417.
https://doi.org/10.1016/j.applthermaleng.2016.07.149

Chu, W. X., Bennett, K., Cheng, J., Chen, Y. T., and Wang, Q. W., 2019, "Thermo-Hydraulic Performance of Printed Circuit Heat Exchanger with Different Cambered Airfoil Fins," *Heat Transfer Engineering*, **41**(8), 708-722.
https://doi.org/10.1080/01457632.2018.1564203

Cui, X. Y., Guo, J. F., Huai, X. L., Cheng, K. Y., Zhang, H. Y., and Xiang, M. R., 2018, "Numerical Study on Novel Airfoil Fins for Printed Circuit Heat Exchanger Using Supercritical CO_2," *International Journal of Heat and Mass Transfer*, **121**, 354-366.
https://doi.org/10.1016/j.ijheatmasstransfer.2018.01.015

Dang, C., and Hihara, E., 2004, "In-Tube Cooling Heat Transfer of Supercritical Carbon Dioxide. Part 1. Experimental Measurement," *International Journal of Refrigeration*, **27**(7), 736-747.
https://doi.org/10.1016/j.ijrefrig.2004.04.018

Kim, D. E., Kim, M. H., Cha, J. E., and Kim, S. O., 2008, "Numerical Investigation on Thermal-Hydraulic Performance of New Printed Circuit Heat Exchanger Model," *Nuclear Engineering and Design*, **238**(12), 3269-3276.
https://doi.org/10.1016/j.nucengdes.2008.08.002

Fan, Y. L., and Luo, L. G., 2008, "Recent Applications of Advances in Microchannel Heat Exchangers and Multi-Scale Design Optimization," *Heat Transfer Engineering*, **29**(5), 461-474.
https://doi.org/10.1080/01457630701850968

Fei, X. Ma T., Chen, Y. T., and Wang, Q. W., 2018, "Two-Dimensional Chemical Etching Process Simulation for Printed Circuit Heat Exchanger Reay, D., Ramshaw, C., and Harvey, A., 2013, *Process Intensification: Engineering for Efficiency, Sustainability and Flexibility: Second Edition*, Butterworth-Heinemann, United Kingdom.
https://doi.org/10.1016/B978-0-08-098304-2.00002-X

Smil, V., 2015, *Natural Gas: Fuel for the 21st Century*, John Wiley & Sons, United Kingdom.

Channels Based on Cellular Automata Model," *Heat Transfer Engineering*, **39**(7/8), 617-629.
https://doi.org/10.1080/01457632.2017.1325660

Fan, J. X., and Yeom, E., 2022, "Numerical Investigation on Thermal Hydraulic Performance of Supercritical LNG in PCHEs With Straight, Zigzag, and Sinusoidal Channels," *Journal of Visualization*, **25**, 247-261.
https://doi.org/10.1007/s12650-021-00804-9

Jiang, Q. F., Pan, C. Y., Guo, T., Tang, Y. B., Gu, J. Y., Aleksandr, P., and Zhu, Z. G., 2022, "Thermal Hydraulic Characteristics of Trans-critical Natural Gas Flowing Through Staggered S-Shaped Fin Microchannel," *Cryogenics*, **124**, 103491.
https://doi.org/10.1016/j.cryogenics.2022.103491

Jiang, Q. F., Pan, C. Y., Song, X., Wan, S. Q., Wen, H. B., Li, H. B., Zhu, Q., and Fu, B., 2022, "Adaptive Design Methodology of Segmented Non-uniform Fin Arrangements for Trans-Critical Natural Gas in the Printed Circuit Heat Exchanger," *Applied Thermal Engineering*, **216**, 119011.
https://doi.org/10.1016/j.applthermaleng.2022.119011

Lee, D. H., Ha, M. K., Kim, S. Y., and Shin, S. C., 2014, "Research of Design Challenges and New Technologies for Floating LNG," *International Journal of Naval Architecture and Ocean Engineering*, **6**(2), 307-322.
https://doi.org/10.2478/IJNAOE-2013-0181

Lian, J., Xu, D. J., Chang, H. L., Xu, Z. R., Lu, X., Wang, Q. W., and Ma, T., 2021, "Thermal and Mechanical Performance of a Hybrid Printed Circuit Heat Exchanger Used for Supercritical Carbon Dioxide Brayton Cycle," *Energy Conversion and Management*, **245**(3), 114573.
https://doi.org/10.1016/j.enconman.2021.114573

Ma, T., Li, L., Xu, X. Y., Chen, Y. T., and Wang, Q. W., 2015, "Study on Local Thermal-Hydraulic Performance and Optimization of Zigzag-Type Printed Circuit Heat Exchanger at High Temperature," *Energy Conversion and Management*, **104**(3), 55-66.
https://doi.org/10.1016/j.enconman.2015.03.016

Ma, T., Xin, F., Li, L., Xu, X.Y., Chen, Y. T., and Wang, Q. W., 2015, "Effect of Fin-Endwall Fllet on Thermal Hydraulic Performance of Airfoil Printed Circuit Heat Exchanger," *Applied Thermal Engineering*, **89**, 1087-1095.
https://doi.org/10.1016/j.applthermaleng.2015.04.022

Ma, T., Zhang, P., Deng, T. R., Ke, H. B., Lin, Y. S., and Wang, Q. W. 2021, "Thermal-Hydraulic Characteristics of Printed Circuit Heat Exchanger Used for Floating Natural Gas Liquefaction," *Renewable and Sustainable Energy Reviews*, **137**, 110606
https://doi.org/10.1016/j.rser.2020.110606

Ngo, T. L., Kato, Y., Nikitin, K., and Tsuzuki, N., 2006, "New Printed Circuit Heat Exchanger with S-Shaped Fins for Hot Water Supplier," *Experimental Thermal and Fluid Science*, **30**(8), 811-819.
https://doi.org/10.1016/j.expthermflusci.2006.03.010

Popov, D., Fikiin, K., Stankov, B., Alvarez, G., Damas, A., Evans, J., and Brown, T., 2019, "Cryogenic Heat Exchangers for Process Cooling and Renewable Energy Storage: a Review," *Applied Thermal Engineering*, **153**, 275-290.
https://doi.org/10.1016/j.applthermaleng.2019.02.106

Tang, L. H., Zeng, M., and Wang, Q. W., 2009, "Experimental and Numerical Investigation on Air-Side Performance of Fin-and-Tube Heat Exchangers with Various Fin Patterns," *Experimental Thermal and Fluid Science*, **33**(5), 818-827.
https://doi.org/10.1016/j.expthermflusci.2009.02.008

Tang, L. H., Cao, Z., and Pan, J., 2020, "Investigation on the Thermal-Hydraulic Performance in a PCHE with Airfoil Fins for Supercritical LNG Near the Pseudo-Critical Temperature under the Rolling Condition,"

Applied Thermal Engineering, **175**, 115404.
https://doi.org/10.1016/j.applthermaleng.2020.115404

Tsuzuki, N., Kato, Y., and Ishiduka, T., 2007, "High Performance Printed Circuit Heat Exchanger," *Applied Thermal Engineering*, **27**(10), 1702-1707.
https://doi.org/10.1016/j.applthermaleng.2006.07.007

Versteeg, H. K., and Malalasekera, W., 2007, *An Introduction to Computational Fluid Dynamics: The Finite Volume Method*, Pearson Education, London, UK.

Wang, Q. W., Chen, Q. Y., Wang, L., Zeng, M., Huang, Y. P., and Xiao, Z. J., 2007, "Experimental Study of Heat Transfer Enhancement in Narrow Rectangular Channel with Longitudinal Vortex Generators," *Nuclear Engineering and Design*, **237**(7), 686-693.
https://doi.org/10.1016/j.nucengdes.2006.09.003

Won, W., Lee, S. K., Choi, K., and Kwon, Y., 2014, "Current Trends for the Floating Liquefied Natural Gas (FLNG) Technologies," *Korean Journal of Chemical Engineering*, **31**,732-743.
https://doi.org/10.1007/s11814-014-0047-x

Wang, L. B., Tao, W. Q., and Wang, Q. W., 2001, "Experimental Study of Developing Turbulent Flow and Heat Transfer in Ribbed Convergent/Divergent Square Ducts," *International Journal of Heat and Fluid Flow*, **22**(6), 603-613.
https://doi.org/10.1016/S0142-727X(01)00127-8

Xu, X. Y., Ma, T., Li, L., Zeng, M., Chen, Y. T., Huang, Y. P., and Wang, Q. W., 2014, "Optimization of Fin Arrangement and Channel Configuration in an Airfoil Fin PCHE for Supercritical CO_2 Cycle," *Applied Thermal Engineering*, **70**(1), 867-875.
https://doi.org/10.1016/j.applthermaleng.2014.05.040

Xu, X. Y., Wang, Q. W., Li, L., Ekkad, S. V., and Ma, T., 2015, "Thermal-Hydraulic Performance of Different Discontinuous Fins Used in a Printed Circuit Heat Exchanger for Supercritical CO_2," *Numerical Heat Transfer Part A Applications*, **68**(10), 1067-1086.
https://doi.org/10.1080/10407782.2015.1032028

Xu, Z. R., Chen, W.N., Lian, J., Yang, X. W., Wang, Q. W., Chen, Y. T., and Ma, T., 2022, "Study on Mechanical Stress of Semicircular and Rectangular Channels in Printed Circuit Heat Exchangers," *Energy*, **238** 121655.
https://doi.org/10.1016/j.energy.2021.121655

Yoon, S. H., Cheon, N. H., and Kang, G. B., 2014, "Assessment of Straight, Zigzag, S-Shape, and Airfoil PCHEs for Intermediate Heat Exchangers of HTGRs and SFRs," *Nuclear Engineering and Design*, **270**(4), 334-343.
https://doi.org/10.1016/j.nucengdes.2014.01.006

Yu, B., Nie, J. H., Wang, Q. W., and Tao, W. Q., 1999, "Experimental Study on the Pressure Drop and Heat Transfer Characteristics of Tubes with Internal Wave-Like Longitudinal Fins," *Heat and Mass Transfer*, **35**(1), 65-73.
https://doi.org/10.1007/s002310050299

Zhao, Z. C., Zhou, Y. M., Ma, X. L., Chen, X. D., Li, S. L., and Yang, S., 2019, "Numerical Study on Thermal Hydraulic Performance of Supercritical LNG in Zigzag-Type Channel PCHEs," *Energies*, **12**(3), 548.
https://doi.org/10.3390/en12030548